remote sensing

MDPI

Article

Near-Surface Dispersion and Current Observations Using Dye, Drifters, and HF Radar in Coastal Waters

Keunyong Kim [1], Hong Thi My Tran [2], Kyu-Min Song [3], Young Baek Son [4], Young-Gyu Park [3], Joo-Hyung Ryu [1], Geun-Ho Kwak [1] and Jun Myoung Choi [2,*]

[1] Korea Ocean Satellite Center, Korea Institute of Ocean Science & Technology, Busan 49111, Republic of Korea; keunyong@kiost.ac.kr (K.K.); jhryu@kiost.ac.kr (J.-H.R.); ghkwak@kiost.ac.kr (G.-H.K.)
[2] Department of Ocean Engineering, College of Environmental and Marine Sciences and Technology, Pukyong National University, Busan 48513, Republic of Korea; 202156838@pukyong.ac.kr
[3] Ocean Circulation & Climate Research Department, Korea Institute of Ocean Science and Technology, Busan 49111, Republic of Korea; kmsong@kiost.ac.kr (K.-M.S.); ypark@kiost.ac.kr (Y.-G.P.)
[4] Tropical & Subtropical Research Center, Korea Institute of Ocean Science & Technology, Jeju 63349, Republic of Korea; sonyb@kiost.ac.kr
* Correspondence: jmchoi@pknu.ac.kr

Abstract: This study explores the near-surface dispersion mechanisms of contaminants in coastal waters, leveraging a comprehensive method that includes using dye and drifters as tracers, coupled with diverse observational platforms like drones, satellites, in situ sampling, and HF radar. The aim is to deepen our understanding of surface currents' impact on contaminant dispersion, thereby improving predictive models for managing environmental incidents such as pollutant releases. Rhodamine WT dye, chosen for its significant fluorescent properties and detectability, along with drifter data, allowed us to investigate the dynamics of near-surface physical phenomena such as the Ekman current, Stokes drift, and wind-driven currents. Our research emphasizes the importance of integrating scalar tracers and Lagrangian markers in experimental designs, revealing differential dispersion behaviors due to near-surface vertical shear caused by the Ekman current and Stokes drift. During slow-current conditions, the elongation direction of the dye patch aligned well with the direction of a depth-averaged Ekman spiral, or Ekman transport. Analytical calculations of vertical shear, based on the Ekman current and Stokes drift, closely matched those derived from tracer observations. Over a 7 h experiment, the vertical diffusivity near the surface was first observed at the early stages of scalar mixing, with a value of 1.9×10^{-4} m^2/s, and the horizontal eddy diffusivity of the dye patch and drifters reached the order of 1 m^2/s at a 1000 m length scale. Particle tracking models demonstrate that while HF radar currents can effectively predict the trajectories of tracers near the surface, incorporating near-surface currents, including the Ekman current, Stokes drift, and windage, is essential for a more accurate prediction of the fate of surface floats.

Keywords: surface current; contaminant dispersion; dye; drifter; HF radar

Citation: Kim, K.; Tran, H.T.M.; Song, K.-M.; Son, Y.B.; Park, Y.-G.; Ryu, J.-H.; Kwak, G.-H.; Choi, J.M. Near-Surface Dispersion and Current Observations Using Dye, Drifters, and HF Radar in Coastal Waters. *Remote Sens.* **2024**, *16*, 1985. https://doi.org/10.3390/rs16111985

Academic Editor: Kaoru Ichikawa

Received: 7 April 2024
Revised: 23 May 2024
Accepted: 28 May 2024
Published: 31 May 2024

1. Introduction

The precise collection of surface current observations is crucial for addressing a spectrum of contemporary issues, including climate forecasting [1,2], oceanic predictions [3,4], environmental incidents [5], and understanding the mechanisms driving contaminant dispersion [6,7]. By merging observations of surface currents with scalar tracers (e.g., dye), it is possible to simulate the distribution of marine pollutants as influenced by surface currents. Gathering surface current observations through an array of incorporated platforms, encompassing both Eulerian and Lagrangian methods, alongside tracer observations from satellites, drones, and in situ observational platforms, presents a robust method for examining the significant role of surface currents on pollutant dispersion. These efforts

are instrumental in deciphering the physical mechanisms and enhancing the accuracy of predictive models.

Drifters, high-frequency (HF) radar, and ocean color imagery are widely used for estimating surface currents. Drifters, passive devices tracked by satellite, provide direct measurements of surface currents, reflecting the movements of water parcels at the ocean's surface within a Lagrangian reference frame. Consequently, they have been instrumental in monitoring ocean circulations across various water bodies, from lakes and coastal areas to open oceans, moving passively with the surface current [8–12]. This platform has been proven to be an effective means of quantifying horizontal dispersion [13,14] and validating ocean models [15,16]. HF radar offers a comprehensive view, capable of mapping surface currents over wide areas from land-based stations, thus providing data for nearshore regions. Ocean color imagery, derived from platforms like the Geostationary Ocean Color Imager (GOCI) and Himawari satellites, provides indirect estimates of surface currents by tracking the movement of chlorophyll-a, sediments, and other scalar products that induce color changes in extensive surface water areas [17,18]. Both HF radar and satellite-based current provide observations in a Eulerian reference frame, which allows for the comprehensive analysis of surface current patterns and predicting contaminant movements [19,20].

Scalar tracers have been used to elucidate the fate of contaminants and quantify mixing in water bodies that respond to currents at various depths [21,22]. Rhodamine water tracer (WT), a water-soluble dye known for its strong fluorescence, has been widely used in investigating water movement and mixing processes across diverse aquatic environments [23–25]. The visibility and detectability of rhodamine WT at low concentrations afford a significant advantage in characterizing the dispersion rate in surface waters [26,27] and deep waters [28] in both horizontal [29] and vertical directions [24,30]. Advances in drone technology have further bolstered observation capabilities, enabling high-resolution aerial imagery collection to track dye movement across temporal and spatial scales [31–33]. The incorporation of traditional field sampling, involving the collection of water samples, with remote sensing methods, can increase the frequency of observations. Moreover, data from in situ sampling can be utilized to calibrate remote sensing data, thus enhancing both the quality and quantity of the data collected.

The near-surface current significantly influences the spread of scalar dispersion at the early dispersion stage within the top surface layer, affected by various physical processes including the Ekman current, Stokes drift, and wind-induced surface currents. Stemming from the interplay between wind force, the Coriolis effect, and viscous drag in the upper ocean layers, the Ekman current induces a depth-dependent vertical velocity profile, known as the Ekman spiral. The depth-averaged Ekman spiral in the surface layer aligns at 45 degrees clockwise relative to the prevailing wind in the Northern Hemisphere [34,35]. Additionally, Stokes drift, driven by wave dynamics, plays a crucial role in the horizontal transport of materials within the top surface layer, facilitating the net transport of water particles along the wave propagation path across consecutive wave cycles [36]. Consequently, wind energizes vertical current shear within the top surface layer by combining effects, including both the Ekman current and Stokes drift, with wind impacts reaching several meters down in coastal regions. Given the rapid vertical diffusion of scalar tracers near the surface, high-resolution observation at the early dispersion stage is essential for precisely analyzing the dispersion mechanisms of scalar tracers driven by the physical processes prevalent in the top surface layer. Enhanced insight into these processes also aids in developing more effective response mechanisms to environmental incidents, such as oil spills and chemical discharges.

In this study, we investigated the temporal evolution of the surface-released dye distribution in a coastal area over half a semidiurnal cycle, focusing on characterizing the dispersion mechanism driven by physical processes in the uppermost layer. We utilized drone, polar-orbital satellite imagery, and in situ sampling techniques to monitor the horizontal temporal dynamics of the dye patch, while vertical diffusivity was estimated using

fluorometer casts. Concurrently, Eulerian surface currents were tracked via HF radar, and Lagrangian surface currents were observed using floats and drifters. By combining observations of the dye patch with surface currents, our aim was to explore the influence of surface physical processes on dispersion rates and the fate of the tracer at the early dispersion stage, providing insights for the development of accurate predictions of marine contaminants.

2. Materials and Methods

2.1. Field Experiment

The dye release and monitoring experiment was carried out aboard the R/V Research 1, a 390-ton vessel, during a cruise on 26 September 2021 [37]. Observations of the dye commenced at 9:10 a.m. and ended at 4:10 p.m. on the same day. The research area was selected off the coast of Yeosu City (Figure 1), situated on the southern boundary of South Korea. Positioned approximately 10 km from the nearest coast, this area lies within the coverage of HF radar (shaded area in Figure 1b), chosen to minimize disruptions from commercial and cargo ship traffic.

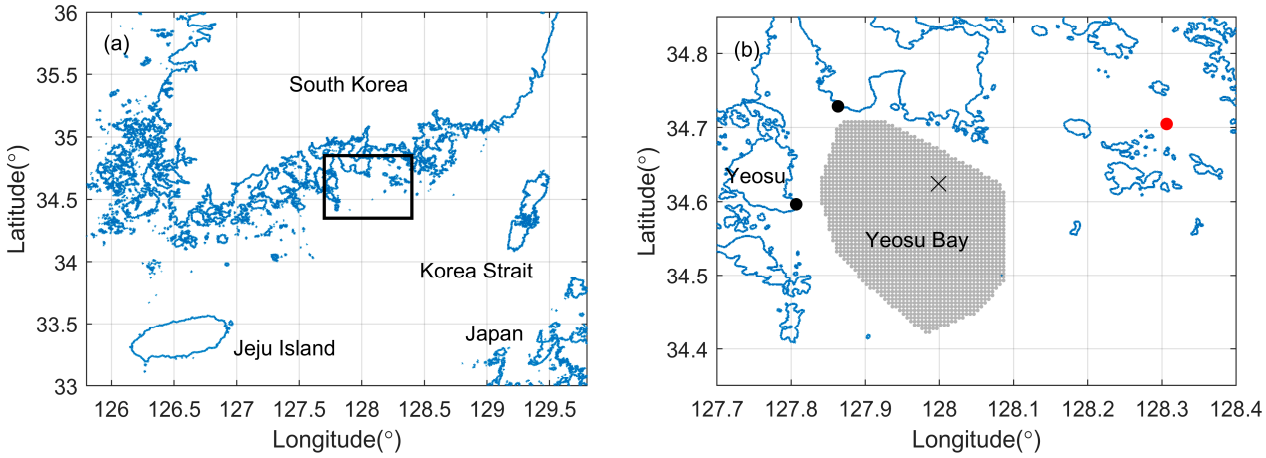

Figure 1. Study area. The domain of (**b**) indicates the area within a rectangle in (**a**). The gray-shaded area represents the coverage of HF radar in Yeosu Bay. The 'x' marks the initial dye release location. The red dot denotes the nearby buoy location where wind and wave data were collected. The black dots denote the locations of two HF radars.

Throughout the experiment, the average wind speed was recorded at 4.87 m/s, with the southward wind speed (4.50 m/s) significantly exceeding the westward wind speed (0.91 m/s) (Figure 2a). The corresponding average wind stress (τ) was calculated at 0.04 Pa (Figure 2b), based on the drag coefficient parameterized by $C_d = (0.8 + aU_{10}) \times 10^{-3}$, where a = 0.065 s/m [38]. The significant wave height, measured by a buoy located 30 km from the dye release point, was approximately 0.2 m (Figure 2c). Since this buoy was positioned behind an intervening island, the wave height at the experiment location would be slightly higher than 0.2 m. The field experiment, encompassing observations of both the dye patch and surface currents, took place under calm weather conditions marked by light northerly winds and small wave activity.

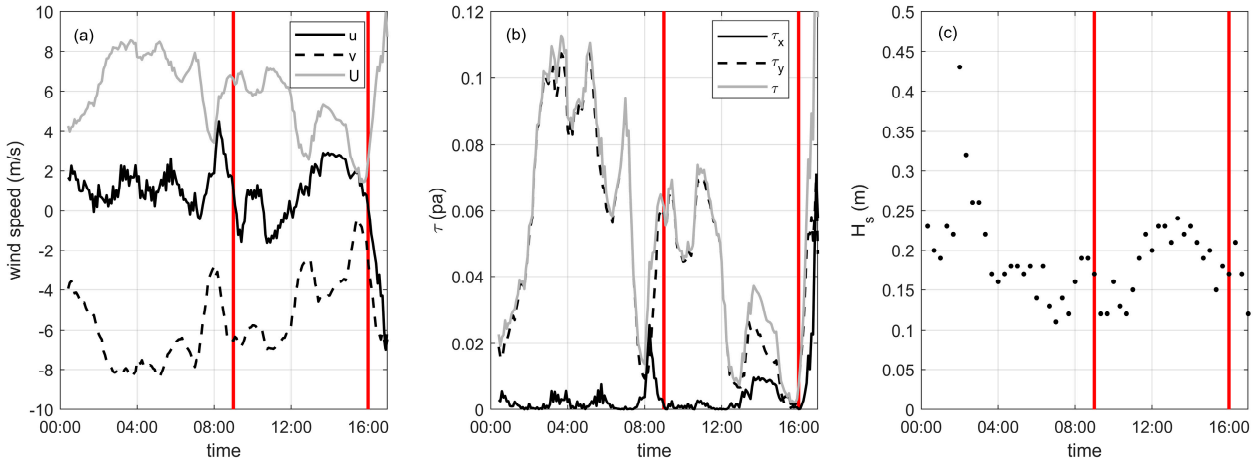

Figure 2. (**a**) Wind speed measured from R/V Research 1 and (**b**) corresponding wind stress. (**c**) Significant wave height as measured by the nearby buoy indicated in Figure 1. The dye monitoring experiment was conducted during the period highlighted by two red lines. Variables u and v represent wind velocities in the east–west (EW) and north–south (NS) directions, respectively, while U denotes the magnitude of wind speed. τ_x and τ_y indicate wind stresses in the EW and NS directions, with τ representing the overall magnitude of wind stress.

2.2. Dye Observations

In the study of early dispersion of a scalar contaminant, rhodamine WT (RWT) dye was chosen as the tracer because of its good water solubility and distinct pink coloration, which facilitates easy detection. The dye was introduced into the ocean surface at the coordinates 34.6302° N, 127.9767° E in Yeosu Bay (Figure 1b), where the water depth was 28 m. To match the density of the dye solution closely with seawater and prevent it from immediately sinking, 38 L of 20% RWT (1150 kg/m^3) was mixed with 17 L of ethanol (789 kg/m^3) and 40 L of in situ seawater (1029 kg/m^3). This mixture resulted in a total volume of 95 L of dye solution with a density of approximately 1015 kg/m^3, slightly lower than that of the surface water. For efficient mixing with the surface water, a diffuser with around 100 holes, each 3 mm in diameter, was used to diffuse the dye. The dye was discharged at a flow rate of 0.2 L/s over a span of 10 min from a floating diffuser located 40 m from the ship, to reduce the disturbance caused by the vessel.

The dye concentration distribution was monitored using both in situ sampling and remote sensing data, including drone and satellite imagery. Measurements spanned a total of 7 h from the start, with the distribution not being measured simultaneously; hence, data from various platforms were incorporated to complete the dispersion time series. From the beginning of the dye release, two drones, a Mavic 2 Pro and an Inspire 2, intermittently captured images of the dye patch, from which concentration estimates were derived from RGB images. These images were then converted to grayscale, featuring separate channels for red, green, and blue, with each pixel in the grayscale image ranging from 0 to 255. Pixels valued below 120 were identified as part of the dye patch, while those exceeding 120 were excluded, which matched well with in situ measurements. Since the images were taken over the ocean, external factors such as waves and the direction of sunlight introduced color variations within the patch. Color filtering might inadvertently omit portions of the patch due to these variations, and linear interpolation was employed to estimate missing pixel values and reconstruct the patch. The ship's dimensions, 46.5 m in length and 9 m in width, served as reference points for distance calibration during image processing to establish pixel dimensions.

To complement drone measurements, two maps depicting the dye distribution at 1 h and 7 h after the release were observed using in situ sampling. The first sampling was conducted by a small boat, measuring 5 m in length, which navigated through the dye patch, collecting surface samples in thirty-five 20 mL plastic bottles over an 18 min period, while GPS coordinates were recorded at the sampling locations. The dye concentrations of the

collected water samples were determined in the laboratory using a Turner Designs 10AU fluorometer (Turner Designs, San Jose, CA, USA). A second sampling was conducted by the R/V Research 1, utilizing an underway system. This system continuously drew surface water from around 2 m depth as the vessel traversed the dye patch in a zigzag pattern for approximately 25 min. The dye concentration was directly measured in real-time by a Turner Designs 10AU fluorometer connected to the underway system on board. The dye concentrations were interpolated using the kriging method to develop a two-dimensional distribution map. The methods of dye preparation, dye sampling, and interpolation were similar to those used in the previous work of Choi et al., 2020 [10].

Additional monitoring of the dye patch was conducted using satellite images from Kompsat-2 (at 10:10 A.M.) and Landsat OLI (at 11:06 A.M.), captured approximately 1 and 2 h after the dye release, respectively. The Kompsat-2 image, supplied by the Korea Aerospace Research Institute (KARI), was an uncorrected 1R file. It underwent geometric correction utilizing Rational Function Coefficients (RPCs), with further corrections made by selecting Ground Control Points (GCPs) using the Landsat OLI image as a reference. The Top of Atmosphere (TOA) radiance was calculated from gain values and subsequently converted to reflectance [39]. The Landsat OLI data, acquired as Level 1 products from the USGS website, received atmospheric correction through the QUAC model in ENVI 5.6.3 software (NV5 geospatial, Broomfield, CO, USA) [40]. To estimate the dye concentration within the satellite imagery, a concentration index was computed using the (red − blue)/(red + blue) formula [41]. Correlation with in situ dye concentrations was established via linear regression, utilizing measurements (n = 24) that coincided with the time of the Landsat OLI capture. Given the 30 m spatial resolution of the Landsat OLI image and the presence of multiple observation points within single pixels, the images were resampled to a 5 m resolution using spline interpolation. A positive correlation was noted between increases in dye concentration and index values, with the index normalized to a 0 to 1 range using min-max scaling [42,43].

The observation platforms were primarily used to monitor the horizontal dispersion of the dye. To capture vertical profiles of dye concentration, a fluorometer attached to a Self-Contained Autonomous Micro-Profiler (SCAMP, Precision Measurement Engineering, CA, USA) was utilized. This sensor records fluorescence emitted by the dye, converting it into voltage readings via a photodiode. The fluorometer operated at a sampling rate of 100 Hz and was set to measure in an upward mode from a depth of 5 m to the surface. For a comprehensive vertical profile, voltage data were binned at 10 cm intervals throughout the profile. In total, nine castings were conducted, resulting in two distinct vertical distribution profiles. Because the sensor exhibits linear sensitivity to fluorescence, the collected voltage data were analyzed to evaluate variances in the vertical distribution of the dye, estimating vertical eddy diffusivity near the surface.

2.3. Surface Current Observations

Concurrently with dye observations, the surface layer current was measured in both Eulerian and Lagrangian reference frames. The Eulerian surface current data, derived from HF radar, were obtained by combining radial data from the Yeosu Harbor area, overseen by the Korea Hydrographic and Oceanographic Agency (KHOA), with additional data from a nearby HF radar installed by the Korea Institute of Ocean Science & Technology (KIOST). The aim of this incorporation was to enhance the accuracy of data within the study area. The synthesis utilized radial data corrected via Antenna Pattern Measurement (APM) conducted through shipboard operations. The CODAR-type ocean radars used in these areas operate on a 25 MHz frequency band, featuring an angular resolution of 5 degrees and a range resolution of 1 km, with a maximum operational range of approximately 45 km. Data from these instruments are averaged over a ±37.5 min period around each hour, with average values reported on the hour. Typically, the surface current measured by HF radar represents the integrated depth within the top 1–2 m [44,45]. When using a 25 MHz frequency band, the integration depth is considered to be about 0.7 m [46].

Lagrangian observations of the surface current were obtained using one float without a drogue and three drifters equipped with drogues at varying depths. These transmitted their GPS coordinates via an Iridium modem at 30 min intervals. The main body (0.9 kg in air) of each device, housing the GPS and battery, was cylindrical, measuring 9 cm in diameter and 16.5 cm in height. For buoyancy, floating materials with outer and inner diameters of 23 and 9 cm, respectively, and a thickness of 6 cm were attached. Drogues (3.3 kg in air), constructed from two intersecting 40 cm plastic plates, were secured to the drifters, setting the average depths of the drogues at 0.6, 0.8, and 1 m, respectively. Approximately 3/4 of the bodies of the floats were submerged, and a steel wire with a diameter of around 0.5 cm was used to tether the float and drogue. The drifters were tracked for one day, primarily to compare their dispersion with the movement of the dye patch.

The Tide Model Driver (TMD) model [47] predicts tidal elevations and velocities at specified locations and times based on harmonic analysis of tidal potentials. It utilizes data from various sources, including satellite altimetry and in situ measurements. We employed the TMD model to estimate tidal currents at the dye release site and compared these calculations with current observations from Eulerian HF radar and Lagrangian drifters.

3. Results

3.1. Surface Current Observations

The observed phases of surface currents, as detected by HF radar and analyzed through the movements of surface drifters, demonstrated strong coherence with the phase of tidal currents. Throughout a 7 h period of monitoring dye distribution, HF radar data revealed a significant shift in current direction due to tide transition. Initially flowing in an east–south direction (Figure 3a), the current later shifted westward, influenced by tidal changes (Figure 3d). The tidal currents, predicted by the TMD model, and the HF radar (HFR) currents at a specific point near the dye release site, showed substantial agreement (Figure 3e,f), with strong correlation coefficients of 0.89 (0.99) for the east–west direction and 0.66 (0.63) for the north–south direction over the day of the experiment (over the experiment interval).

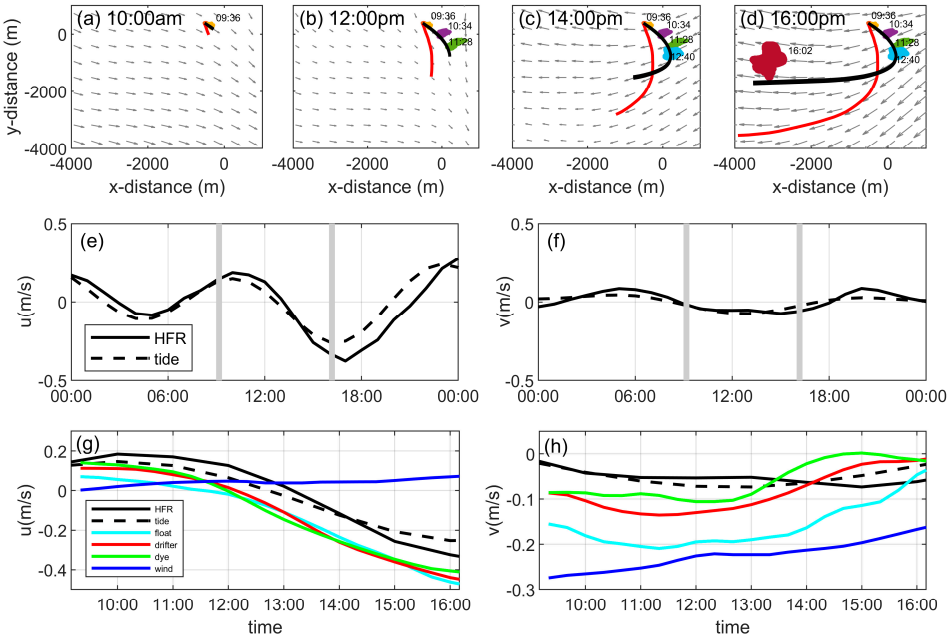

Figure 3. (**a**–**d**) Dye and drifter trajectories overlaid on the background of HF radar current (HFR). Comparison of Eulerian HFR and tidal velocities (modeled from the TMD MATLAB toolbox version 2.5) at a fixed location near the dye release point in the east–west direction (**e**) and north–south direction (**f**). Panels (**g**,**h**) compare the Eulerian velocities in (**e**,**f**) with Lagrangian observational velocities during the experiment duration, marked by two gray lines in (**e**,**f**). Wind speeds in (**g**,**h**) are scaled down by a factor of 20.

When examining the Lagrangian velocities of the three different tracers (dye, float, and drifter), their movements in the EW direction appeared similar and aligned with the Eulerian surface current (Figure 3g). However, in the NS direction, the velocities of the tracers showed variation and differed from the Eulerian surface current (Figure 3h). This disparity was primarily attributed to the influence of relatively strong northerly winds, leading to differential responses among the tracers based on their effective depths. The correlation coefficients between the drifter velocity and the HF radar current, as well as between the drifter velocity and the tidal current, were 0.68 and 0.61, respectively (Figure 3e,f). Similarly, the correlation coefficients for the float velocity with both the HF radar current and the tidal current were 0.61 and 0.77, respectively. The tracking data demonstrate a cohesive movement pattern between the observed Eulerian surface currents and the Lagrangian velocities of the tracers.

3.2. Horizontal Tracer Behaviors

The horizontal advection of the three tracers exhibited distinct behaviors despite being subjected to the same current. The center of the dye patch, influenced by currents at various depths, showed the least displacement, while the float, situated on the surface, exhibited the most significant movement. The three drifters, positioned at slightly varying depths, displayed moderate displacement with minimal relative dispersion among themselves. This variation in advection, especially in the north–south direction, is depicted in Figure 4a, where the central positions of the dye, drifters, and float are connected by lines. The relative displacement among those points was small (~500 m) in the EW direction (see Figure 4b) at the end of the observation period. However, in the NS direction, these points experienced large variation in displacement, approximately 1500 m, 2000 m, and 4000 m, respectively, from their release point (see Figure 4c). The final positions of the three different tracers aligned almost linearly in a direction that subtly deviated rightward from the prevailing southward-blowing wind, but the deviation angle of the dye–drifter line was larger than that of the drifter–float line (Figure 3a). Although the Ekman spiral develops over the surface layer, the wind-driven current was more apparent closer to the surface, as shown by the drifter–float line, which slightly deviated from the southward wind direction. Ekman transport, or the depth-averaged Ekman spiral, was more clearly demonstrated by the slightly deeper currents, as indicated by the dye–drifter lines that deviated more from the wind direction (Figure 3a).

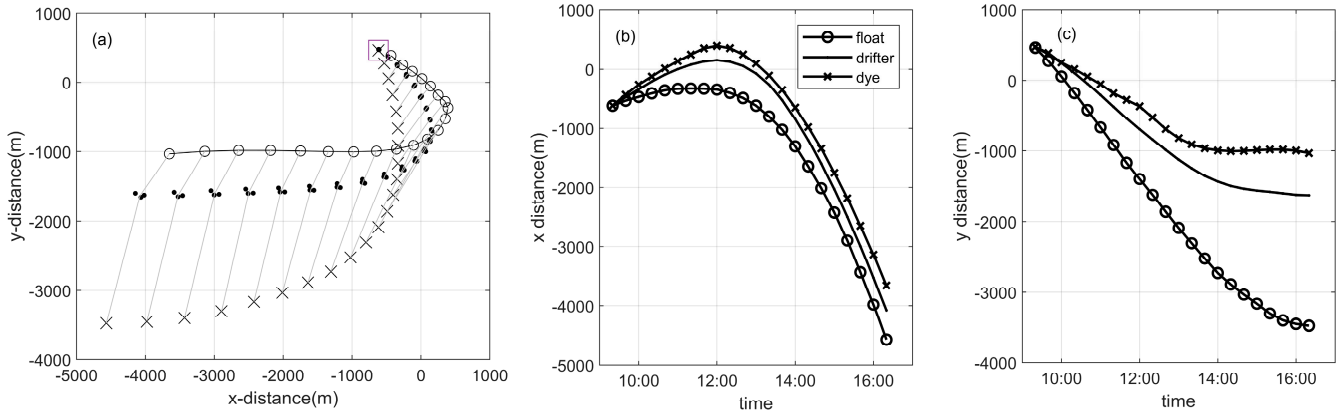

Figure 4. (**a**) Displacement of the center of the dye patch ('○'), float ('×'), and drifters ('·'). The square indicates the release location, and the three concurrent locations are connected by lines. Displacements in the east–west direction (**b**) and north–south direction (**c**).

Employing drones, satellites, and in situ sampling, we observed a biased dispersion direction, as determined by principal axis analysis [48,49]. The variance of dye concentration distribution was calculated using $\sigma_{ij}^2 = \iint (x_i - x_{ci})(x_j - x_{cj})c(x,y)dxdy / \iint c(x,y)dxdy$,

where $x_{ci} = \iint x_i c(x,y)dxdy / \iint c(x,y)dxdy$ and $c(x,y)$ denotes the spatial concentration field of the dye patch at a given time. The i and j represent the x and y dimensions of the dye patch, respectively. From these calculated variances in the x and y directions, the standard deviations along the major (σ_{ma}) and minor (σ_{mi}) principal axes were determined from the eigenvalues of the covariance matrix, with the matrix's eigenvectors providing the orientation of the principal axes. The temporal evolution of variances in both x (EW) and y (NW) directions, along with the major and minor axes and their clockwise angles relative to the southward direction, are tabulated in Table 1.

Table 1. Temporal variations in variance and orientation (clockwise relative to the southward direction) of the dye patch.

#	Time	Source	σ_x (m)	σ_y (m)	σ_{ma} (m)	σ_{mi} (m)	Angle (°)
1	09:10	drone	14.92	24.26	7.93	27.35	−32.89
2	09:26	drone	26.34	23.71	13.94	32.58	−52.10
3	09:27	drone	26.25	24.81	14.36	33.15	−49.56
4	09:28	drone	26.64	25.22	14.85	33.55	−49.52
5	09:29	drone	26.56	25.84	15.04	33.86	−47.99
6	09:30	drone	26.40	26.43	15.28	34.09	−46.34
7	09:31	drone	27.28	26.83	15.64	34.93	−47.37
8	09:32	drone	27.16	27.02	15.61	34.98	−46.70
9	09:35	drone	27.22	28.04	16.45	35.45	−44.54
10	09:38	drone	27.99	29.02	17.38	36.38	−44.06
11	09:39	drone	28.03	29.28	17.49	36.56	−43.58
12	10:10	satellite	41.17	43.58	25.78	54.12	40.91
13	10:34	drone	52.03	46.53	26.73	64.48	52.97
14	10:38	drone	52.99	49.80	26.96	67.53	42.91
15	10:41	drone	53.47	52.20	26.99	69.68	45.09
16	11:28	drone	86.58	67.35	31.23	105.15	52.62
17	11:44	satellite	61.26	67.25	29.25	86.13	42.08
18	12:40	ship	115.39	91.61	56.17	136.20	29.50
19	13:32	drone	120.63	211.82	81.69	229.66	7.26
20	16:02	ship	193.80	284.35	153.94	307.76	2.00

Figure 5 illustrates the temporal evolution of dye concentration, with an ellipse fitting the dye patch at various times. Following the completion of dye injection, a long dye strip approximately 100 m in length and 20 m in width formed in an east–south to west–north direction (Figure 5a). Initially, the dye distribution showed a broad area of uniform concentration for the first 30 min (Figure 5a–c). Subsequently, by 10:30 a.m., the direction of the elongated dye patch reversed, shifting to an east–north to west–south direction, persisting until 1 p.m. During this phase, rapid shifts in tidal current direction led to a significant decrease in the speed of surface currents, accentuating the relative contribution of wind to the dispersion pattern. The direction of elongation, approximately 45 degrees clockwise relative to the prevailing southward wind, indicates the potential impact of wind on the elongation pattern. After 1 p.m., the tidal current accelerated westward, and the elongation direction became aligned with the northerly wind direction.

Given that HF radar measures surface currents at depths of around 1 m, a layer influenced by various physical processes, it is considered to provide an integrated view of currents that can impact the dispersion of tracers within the thin upper layer. The near-surface shear, which is often not detectable by HF radar currents unless the radar frequency is varied to estimate current velocity at different depths, can play a crucial role in the surface dispersion of contaminants [50,51]. This may account for the observed differences between the distribution of the dye patch and the trajectories of the float and drifters. The positioning of the drifters at the edge of the elongated dye patch suggests that the surface currents affecting the drifter, at approximately 1 m depth, are faster in a southward direction than those influencing the dye spread over a depth of 5 m. Moreover, the fact that the float, located at roughly 0.1 m depth, moved farther south than the drifters

indicates that currents at 0.1 m depth are faster southward than those at lower depths. This implies the presence of strong vertical shear closer to the surface.

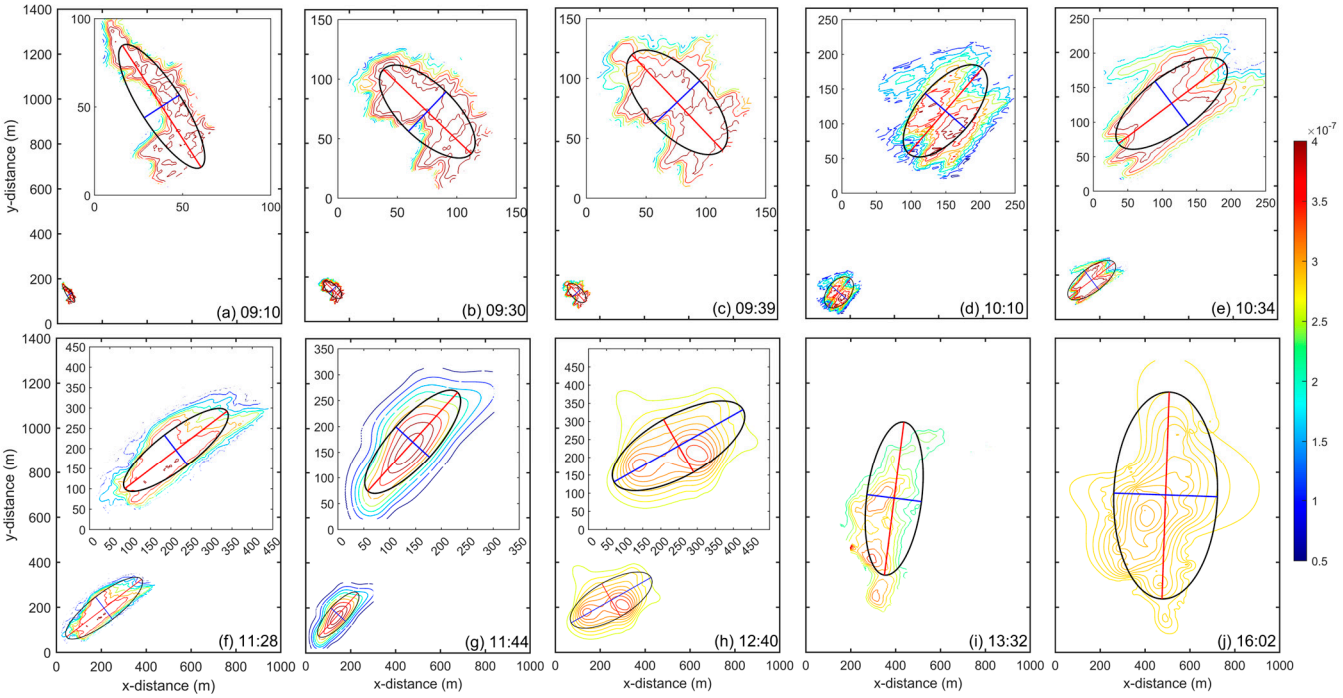

Figure 5. Temporal evolution of the dye patch distribution at different times, with size and direction of the ellipse calculated from the principal axis analysis. The ellipse comprises two axes: the length of the longer axis is $3\sigma_{ma}$ and that of the shorter axis is $3\sigma_{mi}$. The angle, measured from the southward direction rotating clockwise, is presented in Table 1. The actual size of all distributions can be estimated along the x and y axes, with insets providing magnified views of the distributions.

3.3. Vertical Dye Distribution

Two vertical concentration distributions of the dye patch were assessed using a fluorometer mounted on the SCAMP (Figure 6). The initial profile was captured 10 min after dye release was completed, and the subsequent profile was recorded 4 h later. The first vertical distribution revealed a peak concentration just below the surface, likely due to the slightly higher density of the dye solution compared to the surface water. Conversely, the second vertical distribution showed a peak at the surface. A Gaussian fitting was applied to the first profile and adapted for the second by assuming a distribution mirrored with respect to the surface. This analysis yielded standard deviations of 1.39 m and 2.72 m for the vertical dye distribution in the first and second profiles, respectively. The difference between the variance of the later profile (σ_f^2) and of the earlier profile (σ_0^2) is used to calculate the vertical eddy diffusivity $K_z = 0.5\left(\sigma_f^2 - \sigma_0^2\right)/\Delta t$, which was determined to be 1.91×10^{-4} m^2/s with 95% confidence bounds of (1.87, 1.95) $\times 10^{-4}$ m^2/s for the Gaussian fitting, where Δt = 4 h. The temperature difference between the surface and a depth of 5 m, measured by the SCAMP, ranged from 0.1 to 0.3 °C during the experiment period.

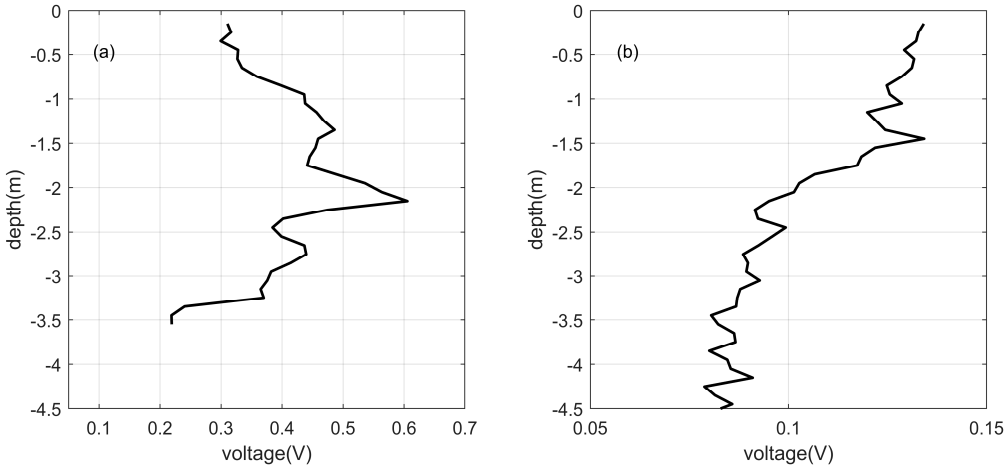

Figure 6. Vertical dye concentration distributions at 10 min (**a**) and 4 h (**b**) after the release, as measured by a fluorometer installed on the SCAMP.

4. Discussion

4.1. Vertical Shear Induced by Near-Surface Dynamics

Dye and drifters constitute an effective experimental pairing for investigating near-surface current dynamics and their influence on surface dispersion. A study has illuminated that dispersion in coastal regions is anisotropic, showcasing marked differences between the dispersion patterns of dyes and drifters, particularly concerning the orientation of wind and surface currents [52]. Additional research on lateral dispersion in a large lake has highlighted that near-surface shear can lead to varying dispersion rates for buoyant versus nonbuoyant pollutants, thus reflecting the distinct behaviors of dyes and drifters [10]. Importantly, vertical shear, propelled by wind forces, has a pronounced impact on the dispersion of dyes and drifters, with dyes, due to their susceptibility to depth-dependent currents, tending to display wider and more segmented dispersion patterns [27]. The wind, which induces the Ekman current and Stokes drift, stands out as the main source of vertical shear affecting horizontal dispersion near the surface.

Our observations indicated that the elongation direction of the dye patch aligned with both the theoretical Ekman current at the surface and the direction of wave propagation, as detected by drone imagery (Figure 7), captured 2.3 h post-release (around 11:30 a.m.), during a period of reduced current speed. The principal axis of the dye patch was deflected approximately 45 degrees relative to the southward direction, coinciding with the wind direction. The directions of waves and wind are not necessarily the same but are closely correlated, typically being almost parallel on average [36,53]. However, we observed the wave direction deviating by 45 degrees from the wind direction. Given that strong winds blew southward for approximately 10 h (see Figure 2) prior to the experiment, this duration is considered sufficient to develop wind-induced waves in a coherent direction due to the short fetch. The relatively large angle (~45 degrees) between the wind and wave directions in our observation might be caused by wave deformation, such as refraction, reflection, and diffraction, due to nearshore geometries. While the reason for the alignment of the wave propagation direction and theoretical Ekman transport direction in the surface layer remains uncertain, our findings suggest that the early biased dispersion behavior of the dye patch in our study can be ascribed to the synergistic effects of the Ekman current and Stokes drift.

To understand this observation further, we performed analytical calculations based on in situ measurements to assess the near-surface vertical shear, thereby estimating the contributions of the Ekman current and Stokes drift components to the observed vertical shear. The Ekman depth $D = \sqrt{2K_z/f}$ [54], where f is the Coriolis parameter, using K_z observed during the experiment, was calculated to be 2 m. This depth signifies the layer in the ocean at which the effect of wind-driven surface currents, influenced by Earth's rotation, markedly

diminishes. The calculated surface currents driven by Ekman flow ($u_{E0} = \tau_x/\rho f$ and $v_{E0} = \tau_y/\rho f$) were approximately 0.20 m/s. Based on the surface current calculation, the Ekman spiral represented as $u_E(z) = u_{E0}e^{-z/D}\cos(z/D - \pi/4) - v_{E0}e^{-z/D}\sin(z/D - \pi/4)$ and $v_E(z) = v_{E0}e^{-z/D}\cos(z/D - \pi/4) + u_{E0}e^{-z/D}\sin(z/D - \pi/4)$ [55] at the vertical transact oriented 45 degrees from the south is depicted in Figure 8. This illustration emphasizes that vertical shear is predominantly concentrated within the upper 5 m. Furthermore, Figure 8 also shows the vertical velocity profile driven by Stokes drift for a monochromatic wave ($U_s(z) = U_{s0}e^{2kz}$) [55]. This velocity profile might be slightly underestimated because the wave height was measured from a buoy located near intervening islands.

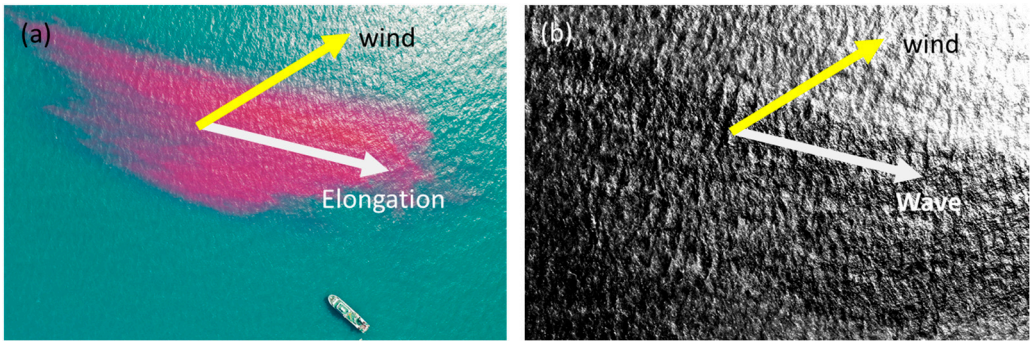

Figure 7. (**a**) Raw RGB images taken by a drone 2.3 h post-dye release (around 11:30 a.m.); (**b**) a magnified segment of (**a**), converted to grayscale to emphasize the wave propagation direction. The angle between the two vectors is approximately 45 degrees.

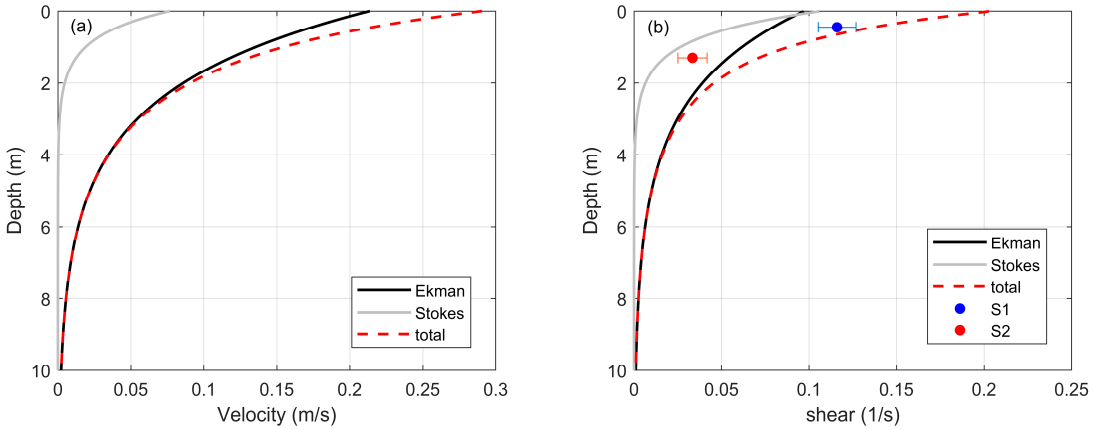

Figure 8. Estimations of near-surface currents driven by the Ekman current and Stokes drift by analytical calculations (**a**) and the corresponding vertical shear (**b**) in the direction of the transect oriented 45 degrees from the southward direction. 'Total' represents the sum of the Ekman and Stokes components. Two dots represent the estimations of mean vertical shear derived from the mean velocity difference between the float and drifters (S1) and between the drifters and dye (S2).

The analytical estimations of vertical shear closely aligned with shear values derived from observations of tracers. By examining velocity differences between the float, positioned at an average depth of around 0.1 m, and the drifters, with an average depth of 0.8 m, the shear was calculated to be 0.12/s. Additionally, analyzing the velocity difference between the drifters and the dye patch, with the dye's average concentration depth around 2 m depth, the shear was estimated to be approximately 0.03/s. The two observations are indicated by two dots in Figure 8b. The time series of shear calculations based on tracers revealed that fluctuations in vertical shear closely followed wind speed variations, with peaks in wind events corresponding to peaks in shear events (Figure 9). This congruence between observed and estimated vertical shear indicates that the early dispersion of dye or

other scalar contaminants released at the surface is markedly influenced by wind-induced vertical shear. The correlation coefficients between wind speed and shear time series were 0.73 and 0.54 for S1 and S2, respectively. Below deeper depths (i.e., below the Ekman depth), the direct effect of wind stress weakens, leading to changes in the current's direction and speed that more closely align with deeper currents such as tidal currents. This can be confirmed by the good response of the dye patch to the tidal current (Figure 3), implying that the impact of wind events can be more pronounced when barotropic tidal currents are minimal.

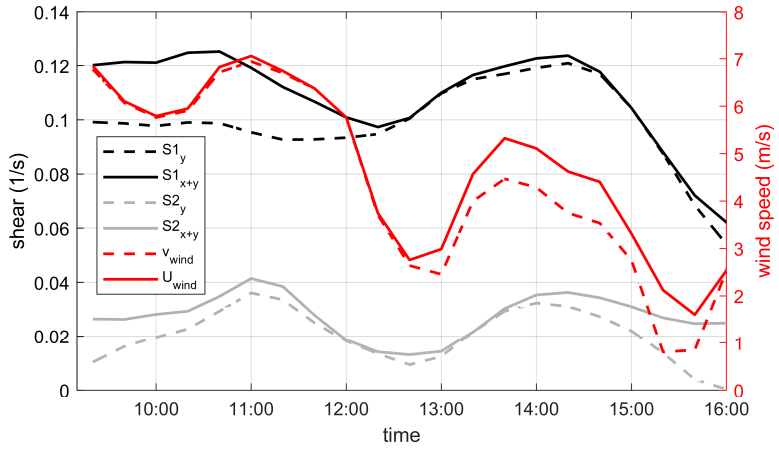

Figure 9. Shear estimation using two tracers (float and drifter). S1 and S2 represent the shear calculated from the velocity difference between the float and drifters (S1) and between the drifters and dye (S2). The subscripts 'y' and '$x + y$' indicate the y direction (north–south or NS) component and the total sum of the NS and east–west (EW) components, respectively. U_{wind} denotes the total wind speed, and v_{wind} represents the NS component of the wind speed. The axis for wind speed is on the right side.

4.2. Horizontal Dispersion and Vertical Mixing of Tracers

Dispersion phases can be delineated by examining the slope of the diffusion diagram [56,57]. Linear increases in the second moment of dye distribution over time $(\sigma^2 \sim t^1)$ signify the diffusive phase, quadratic increases $(\sim t^2)$ denote ballistic dispersion, and cubic increases $(\sim t^3)$ suggest either Richardson dispersion [58] or are indicative of unsteady shear dispersion [59]. Figure 10 illustrates the temporal evolution of horizontal variance (σ^2) for three cases: a dye patch; a combination of a float and three drifters experiencing significant vertical shear; and three drifters subjected to minimal vertical shear. During the 7 h observation period of dye dispersion, the dye patch exhibited distinct dispersion phases. Initially, sub-diffusion $(\sigma^2 \sim t^{0.5})$ was observed for the first 30 min, likely due to restricted dispersion caused by the temporarily buoyant dye patch with a broad, uniform concentration distribution that limited vertical diffusion until the tracer's density matched the surrounding water density. Subsequently, the total variance (σ^2) transitioned to a diffusive phase $(\sim t^1)$, while the variance along the major axis entered a ballistic phase $(\sim t^2)$, suggesting shear dispersion [60] likely driven by vertical shear related to the Ekman current and Stokes drift. This period corresponds to the elongation of the dye patch, with its direction deviating by 45 degrees clockwise from the wind direction. Later, both the variances in major and minor axes exhibited a t^3 slope, indicating a transition to unsteady shear dispersion.

The combined case of float and drifters showed the greatest variance, initially surging with a t^2 slope before persistently ascending at a t^3 slope (red solid line in Figure 10). The early phase of ballistic dispersion $(\sim t^2)$, likely spurred by vertical shear from continuous southward winds, leads to a divergence between the surface current affecting the float and the subsurface currents acting on the drogues connected to the drifters. The dispersion in a major axis may be linked to unsteady shear dispersion $(\sim t^3)$, while the dispersion

in a minor axis followed a diffusive pattern ($\sim t^1$), rendering the total dispersion rate as ballistic, with a t^2 slope $(\sigma^2 \sim \sigma_{ma}\sigma_{mi} \sim t^2)$. As the scale extends to about a kilometer, the float and drifter ensemble engages with large-scale horizontal shear, prompting horizontal shear dispersion. Consequently, at larger scales, the t^3 phase could stem from both unsteady horizontal and vertical shear. The case involving only drifters exhibited the lowest horizontal dispersion rate, reflecting the dye dispersion along the minor axis. The dispersion coefficient $(K = 0.25\,\sigma^2/t)$ of the drifters and the dye patch was observed to be 0.03 m^2/s and 0.2 m^2/s, respectively, at length scales of a few hundred meters. It increased to 1 m^2/s at a length scale of 1 km, as depicted in Figure 10c. For the cases involving a float plus drifters and drifters only, the dispersion coefficients were found to be 5 m^2/s and 0.7 m^2/s, respectively, at a length scale of 1 km. The dispersion coefficient (K) of the dye patch transitioned to a t^3 scaling 2.5 h after release (Figure 10a), corresponding to $K \sim t^2$ (Figure 10b) and $K \sim l^{4/3}$ (Figure 10c) scalings. This phase shift coincided with the dye patch aligning with the direction of the Ekman transport and wave propagation, as depicted in Figure 7. This alignment suggests that the dispersion process of the dye patch can be accelerated by the vertical shear induced by the Ekman current and Stokes drift.

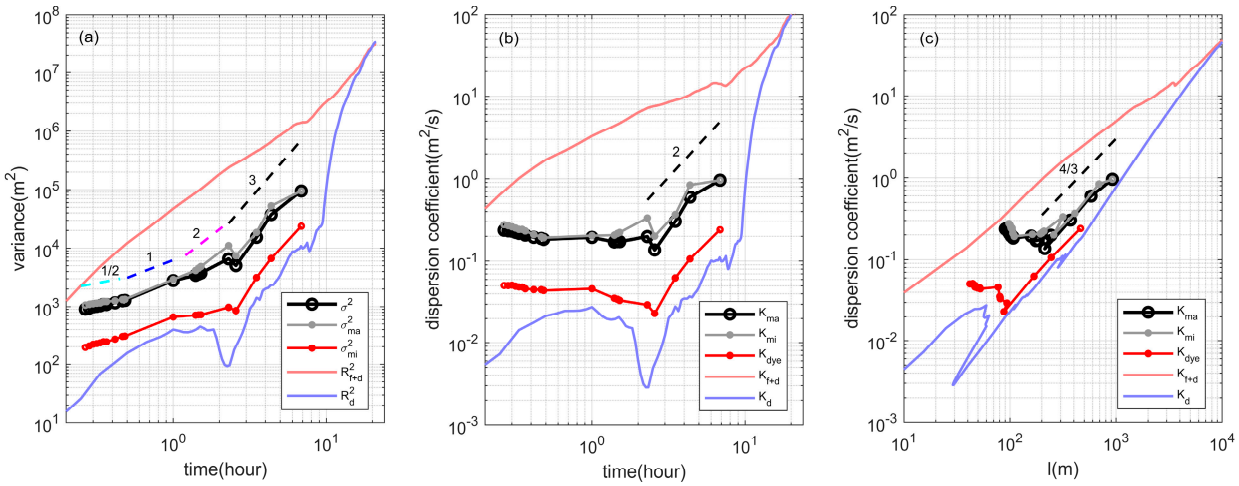

Figure 10. (**a**) Second moments of distribution and (**b**) dispersion coefficient (K) over time for three tracers: a dye patch, a combination of float and drifters ('f + d'), and drifters only ('d'). The total variance (σ^2) of dye concentration distribution is calculated as $(\sigma^2 = 2\sigma_{ma}\sigma_{mi})$, and R^2 represents the relative dispersion of Lagrangian tracers. (**c**) Variation of the dispersion coefficient (K) with the horizontal length scale ($l = 3\sigma$) of dye patch.

The estimation of vertical eddy diffusivity (1.9×10^{-4} m^2/s), which to the best of our knowledge is the first measurement near the ocean surface based on scalar mixing measurements, is an order of magnitude higher than those observed at the base of the ocean mixed layer in the Bay of Bengal as measured by Argo data [61]. Other estimates show K_z in much of the ocean's interior to be around 10^{-5} m^2/s based on scalar mixing and microstructure experiments [21,62–64]. In confined shallow waters, microstructure-based measurements of K_z have ranged from 10^{-5} to 10^{-3} m^2/s in a tropical reservoir [65], around 10^{-4} m^2/s near the surface in Lake Erie [66], and from 1.3×10^{-8} to 8.9×10^{-3} m^2/s in a small lake under various weather and hydrodynamic conditions [67]. Our observations of vertical eddy diffusivity in the weakly stratified top surface layer of the nearshore ocean, under mild weather conditions, were comparable to values observed near the surface in other shallow waters, yet they are an order of magnitude higher than those found in subsurface ocean waters.

By combining near-surface currents from HF radar with analytical calculations of Ekman currents and Stokes drifts, we employed a particle tracking model [68] to forecast tracer paths, as illustrated in Figure 11. Trajectories calculated using HF radar currents

(black line) closely followed those of drifters at an average depth of 0.8 m (dot-dashed line), showcasing HF radar's capability to accurately capture surface currents up to a 1 m depth. However, particle paths intersected the periphery of the wind-elongated dye patch, leading to a slight deviation of trajectories predicted by HF radar from those of the dye patch. This discrepancy arises because the dye patch diffuses across a broader depth, exceeding 5 m, thus affecting its dispersion differently. When the Stokes drift and Ekman current were combined with HF radar data (red line), the combined effect steered particle paths predominantly southwestward. Adding 1% of the wind speed at a height of 10 m (blue line) further refined the particle trajectories, aligning them closely with that of the float (×-dashed line). This variation in tracer paths, influenced by the selection of current components, highlights the critical need for a precise integration of the Ekman current and Stokes drift, alongside a wind effect, to accurately predict the dispersion patterns of tracers with varied characteristics.

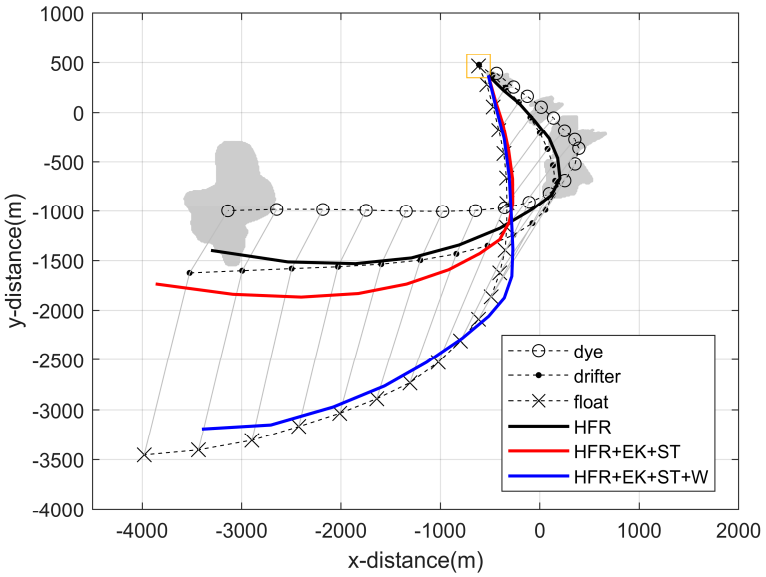

Figure 11. Estimated trajectories from the particle tracking model. HFR, EK, ST, and W indicate current components from HF radar, Ekman current, Stokes drift, and 1% of wind speed, respectively. The gray shaded area indicates the dye patch.

5. Conclusions

This study was motivated by the necessity to understand the mechanisms behind the dispersion of near-surface contaminants such as oil, chemicals, microplastics, and debris in coastal waters, aiming to refine predictive models crucial for environmental management strategies. By employing an approach that combines scalar tracers with Lagrangian markers, we capitalized on the use of both dye and drifters as tracers, alongside modern observational tools like drones, satellites, in situ sampling, and HF radar. This comprehensive methodology led to a thorough examination of the influence of surface currents on contaminant dispersion, emphasizing the vital roles of the Ekman current, Stokes drift, and wind-driven currents in shaping early dispersion behaviors. These physical processes, prevalent in the surface layer, create vertical shear that effectively elongates the dye patch and causes deviations in the velocities of debris on the water surface compared to partially submerged debris. The direction of the dye patch's elongation closely matched the vertical shear induced by the Ekman transport during periods of reduced current velocity. Analytical calculations of vertical shear, on the order of 0.1/s within 1 m depth, guided by the dynamics of the wind-driven current, Ekman current and Stokes drift, closely aligned with tracer movement observations. The movement of the mean locations of the dye patch, drifters, and float demonstrated that the float movement was more closely related to the wind-driven current near the surface, while the dye patch

elongation was more closely associated with Ekman transport. Our experiments revealed the vertical diffusivity rate of 1.91×10^{-4} m^2/s, which was the first scalar mixing-based observation near the ocean surface, and we also observed the horizontal eddy diffusivity of the dye at 1 m^2/s at a length scale of 1000 m. The results of particle tracking models, incorporating various near-surface current data, highlighted the necessity of combining observational data with analytical models for improved predictive accuracy. The movement of drifters at a depth of 0.8 m was well described by the HFR current, while the float, which was closer to the surface, was better depicted by adding wind-driven physical processes. Although the particle tracking results for the dye at relatively deeper depths did not match well with the HFR current and wind-driven processes, the observation of dye patch elongation was possibly influenced by Ekman transport. This approach enhances the ability to predict the fate of tracers by considering the interplay of physical forces in the near-surface layer, enlarging the toolkit available to environmental scientists and policymakers, and supporting more informed decision-making to reduce the impacts of pollution in coastal waters.

Author Contributions: Conceptualization, K.K. and J.M.C.; methodology, K.-M.S., Y.B.S. and Y.-G.P.; software, H.T.M.T.; validation, H.T.M.T. and K.-M.S.; formal analysis, J.M.C. and H.T.M.T.; investigation, J.M.C.; resources, K.-M.S. and K.K.; data curation, Y.B.S. and G.-H.K.; writing—original draft preparation, K.K. and J.M.C.; writing—review and editing, K.K., J.M.C. and Y.-G.P.; visualization, K.K. and J.M.C.; supervision, J.-H.R.; project administration, K.K. and J.-H.R.; funding acquisition, J.-H.R. All authors have read and agreed to the published version of the manuscript.

Funding: This research was supported by Korea Institute of Marine Science & Technology Promotion (KIMST) funded by the Ministry of Oceans and Fisheries (20220407, Korea-China Joint Ocean Research Center). This work was also supported by the Pukyong National University Research Fund (or Pukyong National University Research Foundation, Dongwon Research Foundation) in CD20200854.

Data Availability Statement: The original contributions presented in the study are included in the article, further inquiries can be directed to the corresponding author.

Conflicts of Interest: The authors declare no conflicts of interest.

References

1. Bojinski, S.; Verstraete, M.; Peterson, T.C.; Richter, C.; Simmons, A.; Zemp, M. The concept of essential climate variables in support of climate research, applications, and policy. *Bull. Am. Meteorol. Soc.* **2014**, *95*, 1431–1443. [CrossRef]
2. Du, Y.; Dong, X.; Jiang, X.; Zhang, Y.; Zhu, D.; Sun, Q.; Wang, Z.; Niu, X.; Chen, W.; Zhu, C.; et al. Ocean surface current multiscale observation mission (OSCOM): Simultaneous measurement of ocean surface current, vector wind, and temperature. *Prog. Oceanogr.* **2021**, *193*, 102531. [CrossRef]
3. Röhrs, J.; Sutherland, G.; Jeans, G.; Bedington, M.; Sperrevik, A.K.; Dagestad, K.-F.; Gusdal, Y.; Mauritzen, C.; Dale, A.; LaCasce, J.H. Surface currents in operational oceanography: Key applications, mechanisms, and methods. *J. Oper. Oceanogr.* **2023**, *16*, 60–88. [CrossRef]
4. Aijaz, S.; Brassington, G.B.; Divakaran, P.; Régnier, C.; Drévillon, M.; Maksymczuk, J.; Peterson, K.A. Verification and intercomparison of global ocean Eulerian near-surface currents. *Ocean Model.* **2023**, *186*, 102241. [CrossRef]
5. Shen, Y.-T.; Lai, J.-W.; Leu, L.-G.; Lu, Y.-C.; Chen, J.-M.; Shao, H.-J.; Chen, H.-W.; Chang, K.-T.; Terng, C.-T.; Chang, Y.-C.; et al. Applications of ocean currents data from high-frequency radars and current profilers to search and rescue missions around Taiwan. *J. Oper. Oceanogr.* **2019**, *12*, S126–S136. [CrossRef]
6. Liu, Y.; Harvey, C.M.; Hamlyn, F.E.; Liu, C. Bayesian estimation and reconstruction of marine surface contaminant dispersion. *Sci. Total Environ.* **2024**, *907*, 167973. [CrossRef]
7. Aravind, H.M.; Huntley, H.S.; Kirwan, A.D., Jr.; Allshouse, M.R. Drifter Deployment Strategies to Determine Lagrangian Surface Convergence in Submesoscale Flows. *J. Atmos. Ocean. Technol.* **2024**, *41*, 95–112. [CrossRef]
8. Davis, R.E. Lagrangian ocean studies. *Annu. Rev. Fluid Mech.* **1991**, *23*, 43–64. [CrossRef]
9. Peeters, F.; Wüest, A.; Piepke, G.; Imboden, D.M. Horizontal mixing in lakes. *J. Geophys. Res. Ocean.* **1996**, *101*, 18361–18375. [CrossRef]
10. Choi, J.; Troy, C.; Hawley, N.; McCormick, M.; Wells, M. Lateral dispersion of dye and drifters in the center of a very large lake. *Limnol. Oceanogr.* **2020**, *65*, 336–348. [CrossRef]
11. Subbaraya, S.; Breitenmoser, A.; Molchanov, A.; Muller, J.; Oberg, C.; Caron, D.A.; Sukhatme, G.S. Circling the seas: Design of Lagrangian drifters for ocean monitoring. *IEEE Robot. Autom. Mag.* **2016**, *23*, 42–53. [CrossRef]

12. Berti, S.; Dos Santos, F.A.; Lacorata, G.; Vulpiani, A. Lagrangian drifter dispersion in the southwestern Atlantic Ocean. *J. Phys. Oceanogr.* **2011**, *41*, 1659–1672. [CrossRef]
13. Mantovanelli, A.; Heron, M.L.; Heron, S.F.; Steinberg, C.R. Relative dispersion of surface drifters in a barrier reef region. *J. Geophys. Res. Ocean.* **2012**, *117*, C11016. [CrossRef]
14. Bertin, S.; Sentchev, A.; Alekseenko, E. Fusion of Lagrangian drifter data and numerical model outputs for improved assessment of turbulent dispersion. *EGUsphere* **2024**, preprint. [CrossRef]
15. Van Sebille, E.; van Leeuwen, P.J.; Biastoch, A.; Barron, C.N.; De Ruijter, W.P.M. Lagrangian validation of numerical drifter trajectories using drifting buoys: Application to the Agulhas system. *Ocean. Model.* **2009**, *29*, 269–276. [CrossRef]
16. Muscarella, P.; Carrier, M.J.; Ngodock, H.; Smith, S.; Lipphardt, B.L., Jr.; Kirwan, A.D., Jr.; Huntley, H.S. Do assimilated drifter velocities improve Lagrangian predictability in an operational ocean model? *Mon. Weather. Rev.* **2015**, *143*, 1822–1832. [CrossRef]
17. Choi, J.M.; Kim, W.; Hong, T.T.M.; Park, Y.G. Derivation and evaluation of satellite-based surface current. *Front. Mar. Sci.* **2021**, *8*, 695780. [CrossRef]
18. Hong, T.T.M.; Park, Y.G.; Choi, J.M. Divergence Observation in a Mesoscale Eddy during Chla Bloom Revealed in Submesoscale Satellite Currents. *Remote Sens.* **2023**, *15*, 995. [CrossRef]
19. Dohan, K. Ocean surface currents from satellite data. *J. Geophys. Res. Ocean.* **2017**, *122*, 2647–2651. [CrossRef]
20. Parks, A.B.; Shay, L.K.; Johns, W.E.; Martinez-Pedraja, J.; Gurgel, K.W. HF radar observations of small-scale surface current variability in the Straits of Florida. *J. Geophys. Res. Ocean.* **2009**, *114*, C08002. [CrossRef]
21. Ledwell, J.R.; Watson, A.J.; Law, C.S. Evidence for slow mixing across the pycnocline from an open-ocean tracer-release experiment. *Nature* **1993**, *364*, 701–703. [CrossRef]
22. Sundermeyer, M.A.; Price, J.F. Lateral mixing and the North Atlantic Tracer Release Experiment: Observations and numerical simulations of Lagrangian particles and a passive tracer. *J. Geophys. Res. Ocean.* **1998**, *103*, 21481–21497. [CrossRef]
23. Runkel, R.L. On the use of rhodamine WT for the characterization of stream hydrodynamics and transient storage. *Water Resour. Res.* **2015**, *51*, 6125–6142. [CrossRef]
24. Giraldi, D.; Vitturi, M.D.M.; Zaramella, M.; Marion, A.; Iannelli, R. Hydrodynamics of vertical subsurface flow constructed wetlands: Tracer tests with rhodamine WT and numerical modelling. *Ecol. Eng.* **2009**, *35*, 265–273. [CrossRef]
25. Stride, B.; Abolfathi, S.; Bending, G.D.; Pearson, J. Quantifying microplastic dispersion due to density effects. *J. Hazard. Mater.* **2024**, *466*, 133440. [CrossRef] [PubMed]
26. Upstill-Goddard, R.C.; Suijlen, J.M.; Malin, G.; Nightingale, P.D. The use of photolytic rhodamines WT and sulpho G as conservative tracers of dispersion in surface waters. *Limnol. Oceanogr.* **2001**, *46*, 927–934. [CrossRef]
27. Geyer, N.L.; Balwada, D.; Simons, E.; Speer, K.; Huettel, M. Drifter and dye tracks reveal dispersal processes that can affect phytoplankton distributions in shallow estuarine environments. *Estuar. Coast. Shelf Sci.* **2022**, *269*, 107811. [CrossRef]
28. Richardson, S.D.; Willson, C.S.; Rusch, K.A. Use of rhodamine water tracer in the marshland upwelling system. *Groundwater* **2004**, *42*, 678–688. [CrossRef] [PubMed]
29. Stevens, C.L.; Lawrence, G.A.; Hamblin, P.F. Horizontal dispersion in the surface layer of a long narrow lake. *J. Environ. Eng. Sci.* **2004**, *3*, 413–417. [CrossRef]
30. Mirfenderesk, H.; Hughes, L.; Tomlinson, R. Verification of a three-dimensional advection dispersion model using dye release experiment. In Proceedings of the 16th Australasian Fluid Mechanics Conference, Crown Plaza, Australia, 2–7 December 2007; pp. 233–240.
31. Johansen, K.; Dunne, A.F.; Tu, Y.H.; Almashharawi, S.; Jones, B.H.; McCabe, M.F. Dye tracing and concentration mapping in coastal waters using unmanned aerial vehicles. *Sci. Rep.* **2022**, *12*, 1141. [CrossRef]
32. Burdziakowski, P.; Specht, C.; Dabrowski, P.S.; Specht, M.; Lewicka, O.; Makar, A. Using UAV photogrammetry to analyse changes in the coastal zone based on the sopot tombolo (Salient) measurement project. *Sensors* **2020**, *20*, 4000. [CrossRef] [PubMed]
33. Sibanda, M.; Mutanga, O.; Chimonyo, V.G.P.; Clulow, A.D.; Shoko, C.; Mazvimavi, D.; Dube, T.; Mabhaudhi, T. Application of drone technologies in surface water resources monitoring and assessment: A systematic review of progress, challenges, and opportunities in the global south. *Drones* **2021**, *5*, 84; Erratum in *Drones* **2022**, *6*, 131. [CrossRef]
34. Bressan, A.; Constantin, A. The deflection angle of surface ocean currents from the wind direction. *J. Geophys. Res. Ocean.* **2019**, *124*, 7412–7420. [CrossRef]
35. Constantin, A. Frictional effects in wind-driven ocean currents. *Geophys. Astrophys. Fluid Dyn.* **2021**, *115*, 1–14. [CrossRef]
36. Tamtare, T.; Dumont, D.; Chavanne, C. The Stokes drift in ocean surface drift prediction. *J. Oper. Oceanogr.* **2022**, *15*, 156–168. [CrossRef]
37. Kim, K.; Kim, E.; Choi, J.M.; Shin, J.; Kim, W.; Lee, K.J.; Son, Y.B.; Ryu, J.H. Simulation approach for the tracing the marine pollution using multi-remote sensing data. *Korean J. Remote Sens.* **2020**, *36*, 249–261.
38. Wu, J. Wind-stress coefficients over sea surface near neutral conditions—A revisit. *J. Phys. Oceanogr.* **1980**, *10*, 727–740. [CrossRef]
39. Lee, H.S.; Lee, K.S. Atmospheric correction problems with multi-temporal high spatial resolution images from different satellite sensors. *Korean J. Remote Sens.* **2015**, *31*, 321–330. [CrossRef]
40. Dewi, E.K.; Trisakti, B. Comparing atmospheric correction methods for Landsat OLI data. *Int. J. Remote Sens. Earth Sci. (IJReSES)* **2017**, *13*, 105–120. [CrossRef]
41. Guo, Y.; Wang, H.; Wu, Z.; Wang, S.; Sun, H.; Senthilnath, J.; Wang, J.; Bryant, C.R.; Fu, Y. Modified red blue vegetation index for chlorophyll estimation and yield prediction of maize from visible images captured by UAV. *Sensors* **2020**, *20*, 5055. [CrossRef]

42. Shaheen, H.; Agarwal, S.; Ranjan, P. MinMaxScaler Binary PSO for Feature Selection. In *First International Conference on Sustainable Technologies for Computational Intelligence*; Luhach, A., Kosa, J., Poonia, R., Gao, X.Z., Singh, D., Eds.; Advances in Intelligent Systems and Computing; Springer: Singapore, 2020; Volume 1045. [CrossRef]
43. Jang, W.; Park, Y.; Pyo, J.; Park, S.; Kim, J.; Kim, J.H.; Cho, K.H.; Shin, J.-K.; Kim, S. Optimal band selection for airborne hyperspectral imagery to retrieve a wide range of cyanobacterial pigment concentration using a data-driven approach. *Remote Sens.* **2022**, *14*, 1754. [CrossRef]
44. Rubio, A.; Mader, J.; Corgnati, L.; Mantovani, C.; Griffa, A.; Novellino, A.; Quentin, C.; Wyatt, L.; Schulz-Stellenfleth, J.; Horstmann, J.; et al. HF radar activity in European coastal seas: Next steps toward a pan-European HF radar network. *Front. Mar. Sci.* **2017**, *4*, 8. [CrossRef]
45. Kim, S.Y.; Cornuelle, B.D.; Terrill, E.J. Anisotropic response of surface currents to the wind in a coastal region. *J. Phys. Oceanogr.* **2009**, *39*, 1512–1533. [CrossRef]
46. Stewart, R.H.; Joy, J.W. HF radio measurements of surface currents. In *Deep Sea Research and Oceanographic Abstracts*; Elsevier: Amsterdam, The Netherlands, 1974; Volume 21, pp. 1039–1049.
47. Greene, C.A.; Erofeeva, S.; Padman, L.; Howard, S.L.; Sutterley, T.; Egbert, G. Tide Model Driver for MATLAB. *J. Open Source Softw.* **2024**, *9*, 6018. [CrossRef]
48. Zill, D.G. *Advance Engineering Mathematics*, 3rd ed.; Jones & Bartlett Learning: Burlington, MA, USA, 2020; pp. 418–452.
49. Smith, L.I. *A Tutorial on Principal Components Analysis*; University of Otago: Otago, New Zealand, 2002; pp. 12–20.
50. Laxague, N.J.M.; Özgökmen, T.M.; Haus, B.K.; Novelli, G.; Shcherbina, A.; Sutherland, P.; Guigand, C.M.; Lund, B.; Mehta, S.; Alday, M.; et al. Observations of near-surface current shear help describe oceanic oil and plastic transport. *Geophys. Res. Lett.* **2018**, *45*, 245–249. [CrossRef]
51. Lee, J.H.; Choi, J.M. Measurement of Near-Surface Current Shear Using a Lagrangian Platform and Its Implication on Microplastic Dispersion. *J. Mar. Sci. Eng.* **2023**, *11*, 1716. [CrossRef]
52. Romero, L.; Ohlmann, J.C.; Pallàs-Sanz, E.; Statom, N.M.; Pérez-Brunius, P.; Maritorena, S. Coincident observations of dye and drifter relative dispersion over the inner shelf. *J. Phys. Oceanogr.* **2019**, *49*, 2447–2468. [CrossRef]
53. Clarke, A.J.; Van Gorder, S. The relationship of near-surface flow, stokes drift and the wind stress. *J. Geophys. Res. Ocean.* **2018**, *123*, 4680–4692. [CrossRef]
54. Pedlosky, J. An inertial model of the interaction of Ekman layers and planetary islands. *J. Phys. Oceanogr.* **2013**, *43*, 1398–1406. [CrossRef]
55. Tamura, H.; Miyazawa, Y.; Oey, L.Y. The Stokes drift and wave induced-mass flux in the North Pacific. *J. Geophys. Res. Ocean.* **2012**, *117*, C08021. [CrossRef]
56. Okubo, A. Oceanic diffusion diagrams. In *Deep Sea Research and Oceanographic Abstracts*; Elsevier: Amsterdam, The Netherlands, 1971; Volume 18, pp. 789–802.
57. McWilliams, J.C. Submesoscale currents in the ocean. *Proc. R. Soc. A Math. Phys. Eng. Sci.* **2016**, *472*, 20160117. [CrossRef] [PubMed]
58. Richardson, L.F. I. Some measurements of atmospheric turbulence. *Philos. Trans. R. Soc. Lond. Ser. A Contain. Pap. Math. Phys. Character* **1921**, *221*, 1–28.
59. Fischer, H.B. *Mixing in Inland and Coastal Waters*; Academic Press: Cambridge, MA, USA, 1979.
60. Saffman, P.G. The effect of wind shear on horizontal spread from an instantaneous ground source. *Q. J. R. Meteorol. Soc.* **1962**, *88*, 382–393. [CrossRef]
61. Shee, A.; Sil, S. Estimations of vertical diffusivity and applications on a mixed layer budget analysis of the Bay of Bengal using Argo data. *J. Mar. Syst.* **2023**, *239*, 103857. [CrossRef]
62. Gregg, M.C. Diapycnal mixing in the thermocline: A review. *J. Geophys. Res. Ocean.* **1987**, *92*, 5249–5286.
63. Ledwell, J.R.; Watson, A.J.; Law, C.S. Mixing of a tracer in the pycnocline. *J. Geophys. Res. Ocean.* **1998**, *103*, 21499–21529. [CrossRef]
64. Ledwell, J.R.; St. Laurent, L.C.; Girton, J.B.; Toole, J.M. Diapycnal mixing in the Antarctic circumpolar current. *J. Phys. Oceanogr.* **2011**, *41*, 241–246. [CrossRef]
65. Yang, P.; Xing, Z.; Fong, D.A.; Monismith, S.G.; Tan, K.M.; Lo, E.Y. Observations of vertical eddy diffusivities in a shallow tropical reservoir. *J. Hydro-Environ. Res.* **2015**, *9*, 441–451. [CrossRef]
66. Bouffard, D.; Boegman, L.; Rao, Y.R. Poincaré wave–induced mixing in a large lake. *Limnol. Oceanogr.* **2012**, *57*, 1201–1216. [CrossRef]
67. Masunaga, E.; Itoh, S.; Kitamura, T. Vertical mixing and oxygen flux caused by daily sea breezes in a shallow stratified lake. *Limnology* **2023**, *24*, 95–109. [CrossRef]
68. Jalón-Rojas, I.; Wang, X.H.; Fredj, E. A 3D numerical model to Track Marine Plastic Debris (TrackMPD): Sensitivity of microplastic trajectories and fates to particle dynamical properties and physical processes. *Mar. Pollut. Bull.* **2019**, *141*, 256–272. [CrossRef] [PubMed]